International Journal of Biological Macromolecules 181 (2021) 136–149

Contents lists available at ScienceDirect

International Journal of Biological Macromolecules

journal homepage: http://www.elsevier.com/locate/ijbiomac

Tuning the functional properties of lignocellulosic films by controlling the molecular and supramolecular structure of lignin

E. Gerbin [a], G.N. Rivière [b], L. Foulon [a], Y.M. Frapart [c], B. Cottyn [d], M. Pernes [a], C. Marcuello [a], B. Godon [a], A. Gainvors-Claisse [a], D. Crônier [a], A. Majira [d], M. Österberg [b], B. Kurek [a], S. Baumberger [d], V. Aguié-Béghin [a,*]

[a] Université de Reims Champagne Ardenne, INRAE, FARE, UMR A 614, 51097 Reims, France
[b] Aalto University, School of Chemical Engineering, Department of Bioproducts and Biosystems, P.O. Box 16300, FI-00076 Aalto, Espoo, Finland
[c] Laboratoire de Chimie et Biochimie Pharmacologiques et Toxicologiques—UMR CNRS 8601, Université de Paris, France
[d] Institut Jean-Pierre Bourgin, INRAE, AgroParisTech, Université Paris-Saclay, 78000 Versailles, France

ARTICLE INFO

Article history:
Received 30 January 2021
Received in revised form 13 March 2021
Accepted 13 March 2021
Available online 23 March 2021

Keywords:
Protobind 1000
Colloid lignin particles (CLP)
Cellulose nanocomposite
Antioxidant and antibacterial properties
Phenoxy radicals
Electron paramagnetic resonance

ABSTRACT

This study investigated the relationships between lignin molecular and supramolecular structures and their functional properties within cellulose-based solid matrix, used as a model biodegradable polymer carrier. Two types of derivatives corresponding to distinct structuration levels were prepared from a single technical lignin sample (PB1000): phenol-enriched oligomer fractions and colloidal nanoparticles (CLP). The raw lignin and its derivatives were formulated with cellulose nanocrystals or nanofibrils to prepare films by chemical oxidation or pressure-assisted filtration. The films were tested for their water and lignin retention capacities, radical scavenging capacity (RSC) and antimicrobial properties. A structural investigation was performed by infrared, electron paramagnetic resonance spectroscopy and microscopy. The composite morphology and performance were controlled by both the composition and structuration level of lignin. Phenol-enriched oligomers were the compounds most likely to interact with cellulose, leading to the smoothest film surface. Their RSC in film was 4- to 6-fold higher than that of the other samples. The organization in CLP led to the lowest RSC but showed capacity to trap and stabilize phenoxy radicals. All films were effective against *S. aureus* (gram negative) whatever the lignin structure. The results show the possibility to tune the performances of these composites by exploiting lignin multi-scale structure.

1. Introduction

A considerable effort has been made worldwide to develop new materials from bioresources to replace petroleum-based plastics, which contribute to the acceleration of global warming and plastic pollution. To be competitive, the novel materials must combine several properties, such as low density, renewability, recyclability, processability and compatibility with human health and the environment, and low production cost [1]. Cellulose is the most abundant polymer found in forestry and agricultural biomass, and it meets all of the above requirements and can thus be used as a building block for new biomaterials. Its potential to produce high-performance nanocomposites filled with lignocellulosic fibres (60–70%) has been demonstrated for forty years [2,3]. Moreover, nanocellulose-based products have shown a wide range of potential applications, including engineered tissue for medical purposes, reinforcement fillers in packaging, sensors and flexible electronics, and protective coatings in optical devices. These products involve either cellulose nanocrystals (CNC) prepared by controlled acid hydrolysis of amorphous domains [4] or cellulose nanofibrils (CNF) recovered from mechanical disintegration or steam explosion of fibres [5,6]. Depending on the cellulose source (trees, plants, bacteria, algae, and tunicates) and the process used, the rod-like shape of these nanomaterials varied in length from 100 nm to several μm, with an aspect ratio ranging from 25 to higher than 1000 for CNC and CNF, respectively [7,8]. Both CNC and CNF represent attractive materials in the nanotechnology field [9,10]. Notably, their capacity to be aligned in nanoassemblies is often exploited as an advantage [8,11].

Along with cellulose, lignin is a polymer of interest for biobased materials. It is the second most abundant polymer (15–30%) in lignocellulosic biomass and provides multifunctional compounds with high valorization potential that are available as byproducts from lignocellulose processing in pulping or bioethanol production [12,13]. Lignin is a heterogeneous polymer crosslinked with cellulose and hemicellulose in plant cell walls. Several chemical and enzymatic processes using advanced oxidative reactions have thus been developed to remove this recalcitrant polymer from the cell wall and convert it into aromatic

* Corresponding author at: Université de Reims Champagne Ardenne, INRAE, FARE, UMR A 614, 51097 Reims, France.
E-mail address: veronique.aguie@inrae.fr (V. Aguié-Béghin).

https://doi.org/10.1016/j.ijbiomac.2021.03.081

products of industrial interest [14–16]. Consequently, the chemical characteristics of the isolated raw material differ from those of native lignin based on the type and severity of the removal process. Among those characteristics are the molar mass distribution, content of monomer units, pattern of intermonomer linkages (S, G, H), amount of functional groups (e.g., phenol, alcohol or methoxy groups) [14,17,18], and presence of new groups such as sulfonate groups formed during the process [19]. In addition, the phenolic fraction is more or less contaminated by carbohydrates, which are either solubilized along with lignin or present as a residual fraction after lignocellulose conversion [15,19–21]. Among the different industrial lignin production processes, the alkali (or soda) process has the advantage of not introducing any sulfur in the polymer backbone and preserving some of the lignin's native structure, such as β-aryl ether bonds [12]. Moreover, as an aqueous process, it does not require organic solvents that are detrimental to the environment. One of the most widely studied commercial soda lignins is PB1000 lignin (GreenValue Enterprises, USA) [17,22,23], which is produced from a grass mixture and composed of several percent of free phenolic acids of potential interest. Combining solvent fractionation and ionic liquid treatment has allowed the depolymerization and demethylation of this industrial lignin, thus yielding additional free phenols that promote antioxidant activity in solution [23]. In parallel, water-dispersible lignin nanoparticles (also named colloidal lignin particles, CLP) were developed from kraft, alkaline and organosolv lignins [24]. These studies demonstrate that the lignin structure and supramolecular organization can be adjusted either by fractionation and depolymerization processes or by promoting self-assembly. Moreover, all of these structures may optimize the valorization of the material in higher-value applications, such as in nano- or microcarriers, supercapacitors for energy storage [25], high-performance carbon fibres for microelectronics [26,27], high mechanical performance thermoplastics [28,29], multifunctional cellulose-based films (anti-UV, antireflective, antioxidant in coated or casted films) [22,30–32], antimicrobial or antiviral nanoparticles [33,34] as flocculation agents or stabilizers in Pickering emulsions [35–37], and water reducers for cement admixtures. [38]

Lignin phenolics can be associated with a nanocellulose-based matrix to generate multifunctional composites that combine the mechanical resistance, transparency and barrier properties of nanocellulose with the hydrophobic, anti-UV, antioxidant and cross-linking properties of phenolics [39]. More recently, lignin-carbohydrate complexes have been shown to be promising scavengers of reactive oxygen species and thus are highly sought-after in biomedical applications [40]. In these composite systems, the structural level of lignin might impact the accessibility of its functional groups and consequently the properties of the material, which has not been investigated thus far. Thus, the objective of this study was to explore tuning the lignin organization level and determine the associated impacts on the functional properties of a polysaccharide-based matrix.

For this purpose, a nanocomposite system based on cellulose nanocrystals and nanofibrils was used as a model material, in which PB1000 soda lignin was introduced in different structural forms and under different conditions. The forms include raw lignin, an oligomer fraction, depolymerization products and colloidal lignin particles (CLP). The cellulose-lignin nanocomposites were prepared either after oxidative reaction (using Fenton's reagent) prior to film formation or simply by mechanical mixing with pressure-assisted filtration. These two procedures were selected to apply different crosslinking degrees of the whole system. The paper focuses on two functional properties relevant to food packaging or medical applications: radical scavenging and antibacterial properties. The structure of the composites was investigated through a combination of spectrometric, topographic and physico-chemical sorption methods to assess the functional groups and interactions between cellulose and lignin. This multiple approach allowed us to gain insights into the influence of both the initial molecular structure and supramolecular structure of lignin during film processing on the two functional properties of interest. The results show the importance of analysing the lignin oligomer structure and adopted conformation within the final material to enable the optimization of the final functional properties of the composite material.

2. Materials and methods

2.1. Materials

Technical grass lignin PB1000 was purchased from GreenValue Enterprises LLC (USA) [41]. Fractions F1CH40 and F2CH40 were obtained by two combined solvent fractionation and ionic liquid treatment processes carried out on PB1000 according to a previously published approach [23]. F1CH40 corresponds to the soluble PB1000 ethyl acetate (EA) extract after [HMIM]Br treatment (IL), and F2CH40 corresponds to the EA residue submitted to butanone extraction followed by IL treatment. Each IL treatment was performed in an Ace Pressure tube under an inert atmosphere with conventional heating at 110 °C. After 40 min, the solid residue was filtered and washed with water (20 mL) and EA (20 mL). The filtrate was recovered, the layers were separated, and the aqueous layer was extracted with EA (2 times 20 mL). The combined EA extracts were dried over $MgSO_4$ and concentrated under reduced pressure below 35 °C. The chemical characteristics of the PB1000 and EA fractions after [HMIM]Br treatment are summarized in Table 1. The lignin model compounds (LMCs) [39] included lignin fractions isolated from spruce wood (*Picea abies*) (FL-G) and maize stalks (*Zea mays* L.) (FL-GS), synthetic lignins (DHP-G) and a commercial dimer (guaiacylglycerol-β-guaiacyl ether, G2). The CLPs were prepared from PB1000 according to the procedure described by Rivière et al. [34]. Briefly, 2 g of lignin was dissolved in acetone:water (3/1, v/v – 200 mL) for 3 h under magnetic stirring. The lignin solution was then filtered through a glass microfibre filter grade GF/F (Whatman, Maidstone, United Kingdom) before being poured into 500 mL of water under vigorous stirring. The CLP dispersion was then dialyzed against deionized water to remove the residual acetone (the water was frequently changed). After 4 days, an aqueous CLP dispersion (c.a. 2 wt%) was obtained. Cellulose nanocrystals (CNC) were obtained from ramie fibres (*Boehmeria nivea*) after mild sulfuric acid hydrolysis as previously described [31]. Cellulose nanofibrils (CNF) were prepared from hardwood kraft pulp fibres following the procedure described in [42]. After washing in a sodium formula, the fibres were fibrillated using a type M-110P

Table 1
Characteristics and solvent conditions of PB1000 and its derivatives before cellulose-based film preparation.

Lignin samples	Mw g mol^{-1}	Mn g mol^{-1}	Pd	PhOH mmol g^{-1}	Solvent conditions		Film matrix
					free	with cellulose	
PB1000[a]	1260	1015	6.4	2.7	EtOH/Water 6/4 (v/v)	EtOH/water 3/7 (v/v)	CNC
F1CH40[a]	876	680	4.8	6.6	Dioxan/water 9/1 (v/v)	Dioxan/water 9/11 (v/v)	
F2CH40[a]	872	676	4.7	8.3			
CLP[b]	–	–	–	–	Water		CNC or CNF

[a] Information obtained from [23].
[b] Colloidal particle of lignin prepared according to [34]; and Pd: polymerization degree estimated by using mean Mw value of one phenylpropane unit ($C_9H_9O_2(OCH_3)_{1-2}$), 196 g mol^{-1}.

microfluidizer (Microfluidics, Newton, Massachusetts, U.S.A.) to obtain a CNF suspension (c.a. 2 wt%).

2.2. Particle size and ζ potential

The CLP dispersion was characterized using a Zetasizer Nano-ZS90 (Malvern, United Kingdom). The particle size (referred to as the hydrodynamic diameter) was determined via dynamic light scattering. The ζ potential was determined with a dip cell probe and calculated from the electrophoretic mobility data using a Smoluchowski model. The results are reported as an average of three measurements. One millilitre of the CLP dispersion was used for all measurements with a concentration of c.a. 0.2 g L^{-1}. Two different batches of CLP with similar size distributions and ζ potentials were prepared using the same conditions, and their detailed characterization can be found in the supplementary document (Fig. S1). The ζ potential of CNC in suspension was characterized under the same conditions, and their particle size distribution was measured by atomic force microscopy (AFM) in a previous study [43].

2.3. Preparation of cellulose-lignin films

Cellulose-lignin films were prepared from CNC and CNF according to two procedures: a chemical oxidation procedure with Fenton's reagent [22] or pressure-assisted filtration and drying at ambient temperature (25 °C) and 50% relative humidity (RH), respectively [32]. Mixtures of CNC and lignin were prepared in an ethanol/water mixture (3/7, *v*/v) for PB1000, in dioxane/water (9/11, v/v) for F1CH40 and F2CH40 and in water for CLP to obtain nanocomposite films with 10 or 17 wt% lignin content. The addition of Fenton's reagent was adjusted to a $FeSO_4/H_2O_2$ molar ratio of 10 (1 mM $FeSO_4$, 0.1 mM H_2O_2 or 0.3 mM $FeSO_4$, 0.03 mM H_2O_2) at pH 3 with diluted sulfuric acid to ensure a mild oxidation reaction in each suspension. The mixture was stirred for 2 h at ambient temperature before film preparation by casting onto a horizontal PTFE plate and drying overnight under ambient air and relative humidity. The volume of suspension poured in the PTFE plate was adjusted for each mixture to obtain an average film thickness (CNC-lignin) on the order of 27 ± 3 μm, which was measured with a dual-thickness gauge (Käfer GmbH, Villigen, Germany). The thickness of the nanocomposite films prepared from CNF averaged 80 ± 3 μm. All cellulose-based films were stored under controlled conditions (23 °C, 50% RH) in the dark before testing. In parallel, supported thin films were produced by applying 300 μL of each cellulose-lignin mixture to clean quartz slides (3.1 cm^2) and then drying the slides under ambient conditions overnight. All films were conditioned according to their characterizations.

2.4. Structural and spectroscopic characterizations

2.4.1. Fourier transform infra-red (FTIR) spectrophotometry

FTIR spectra were recorded for each initial lignin and the films using a Nicolet 6700 spectrophotometer (Thermo Scientific, U.S.A.). The tablets were prepared by mixing 200 mg of spectroscopic grade KBr with 3 mg of lignin or crushed film. In the case of CNF-based films, the spectra were recorded by attenuated total reflectance. Each spectrum represented a record of 32 scans at a resolution of 4 cm^{-1} from 400 to 4000 cm^{-1}, and we performed background subtraction, baseline correction and then normalization with respect to the area under the spectrum.

2.4.2. Quantitative ^{31}P NMR

Derivatization of the LMC samples with 2-chloro-4,4,5,5-tetramethyl-1,3,2-dioxaphospholane (Sigma-Aldrich, France) was performed according to [44]. NMR spectra were acquired on a Bruker Biospin Avance III 500 MHz spectrometer. A total of 256 scans were performed with a delay time of 6 s between successive pulses. The spectra were processed using Topspin 3.1 from Bruker Biospin. All spectra were manually phase-corrected and calibrated with the observed signal from the reaction product between water and 2-chloro-4,4,5,5-tetramethyl-1,3,2-dioxaphospholane in pyridine/$CDCl_3$ at 132.2 ppm. Signals were assigned by comparison with the ^{31}P NMR chemical shift range as indicated in [22].

2.4.3. Electron paramagnetic resonance (EPR)

Spectra were recorded at 20 °C using a Bruker 540 EPR spectrometer operating in the X-band (9.85 GHz) under the following conditions: modulation frequency, 100 kHz; modulation amplitude, 10 G; time constant, 327.6 ms; conversion time, 327.91 ms; and microwave power, 10 mW. Data acquisition, processing, and double integration were performed using Bruker software. Approximately 20 mg of crushed film was added to EPR tubes (Wilmad, 707-SQ-100 M). The amplitude of the signal was calculated based on the difference between the maximum and the minimum of the spectral signal, which was possible because the EPR signal was symmetric.

2.4.4. Atomic force microscopy (AFM)

AFM images of cellulose-based films were acquired on a Multimode-8 AFM setup (Bruker, Santa Barbara, CA) in PeakForce tapping mode in air. Images were taken with *V*-shaped silicon nitride ScanAsyst-air AFM probes (nominal spring constant of 0.4 N m^{-1}). Prior to AFM image acquisition, the AFM tip was calibrated. The deflection sensitivity of the AFM probe was achieved by recording at least three force-distance curves on a stiff sapphire flat surface. The spring constant was determined by the thermal tuning method [45]. The nominal sharp tip radius is 2 nm, which minimizes nondesirable broadening effects [46]. AFM images were acquired with a vertical tip oscillation frequency and acquisition rate of 1 kHz and 0.4–0.6 Hz, respectively. The image resolution was defined as 512 × 512 pixels/line. Several images were taken in different scan areas ranging from 400 μm^2 to 25 μm^2 to determine the roughness parameters of the films (Ra) and provide an overview of lignin nanoparticle distribution on each sample. Ra is defined as the arithmetic average of the absolute values of the surface height deviations measured from the mean plane. Roughness parameters will aid in a more complete overview of how lignin nanoparticles are dispersed on the cellulose film surface. Moreover, to precisely quantify the dimensions of lignin features, cross-section profiles were produced (N = 300). Histograms were fitted by Gaussian distribution using OriginPro 8.0 software. Roughness film parameters of the entire AFM images and cross-section lignin profiles were rendered by Nanoscope Analysis 1.8 software.

2.4.5. Dynamic vapor sorption (DVS)

A gravimetric sorption analyser (IGA, Intelligent Gravimetric Analyser, Hiden Isochema Ltd.) was used to measure the water sorption isotherm of each film [47]. An ultrasensitive microbalance located in a thermostatically controlled chamber was used to measure changes in film mass (approximately 4 mg) as low as 0.1 mg at 20 °C and at RH values from 10 to 90%. The film was hydrated stepwise via 10% RH increments during the water vapor sorption and desorption phases, and the mass was recorded until equilibrium at each stage. The water content (C_w) was calculated according to Eq. (1):

$$C_w = \frac{m_{eq} - m_d}{m_d} \times 100 \quad (1)$$

where m_{eq} is the mass of the sample in the equilibrium state and m_d is the mass of the dry sample measured after total drying under a dry flow of nitrogen. Sorption isotherms were analyzed by using the PARK model according to a previous analysis [39,47].

2.5. Antioxidant activity determination

2.5.1. Soluble radical scavenging activity of lignin in solution

The soluble radical scavenging activity of lignin samples was evaluated both in absolute ethanol solution and in water by measuring

their reactivity towards the stable soluble radicals (R•) 2,2-diphényl-1-picrylhydrazyle (DPPH•) [48] and 2,2′-azino-bis(3-ethylbenzothiazoline-6-sulfonic acid radical cation ($ABTS^{\bullet+}$) [49]. Each lignin sample was solubilized in ethanol/water (6/4, v/v) or dioxane/water (9/1, v/v) to obtain concentrations between 0.25 and 0.5 mg mL^{-1}. The dispersion was stirred until total solubilization before its radical scavenging activity was measured.

2.5.1.1. DPPH• test. In a quartz cuvette, 77 μL of lignin solution was added to 3 mL of 60 μM DPPH• in absolute ethanol solution. The absorbance at 515 nm was monitored using a UV–Vis double-beam spectrophotometer (Shimatsu, Japan) until reaching a plateau. A blank was prepared under the same conditions using 77 μL of solvent instead of the lignin sample. The kinetics of radical scavenging were analyzed from at least 5 solutions in the concentration range mentioned above by calculating the difference between the absorbance of the sample and blank solution every 5 and 10 min. The percentage of residual DPPH• was calculated and plotted vs the concentration of soluble lignin in solution.

2.5.1.2. $ABTS^{\bullet+}$ test. ABTS was dissolved in water to a concentration of 7 mM. $ABTS^{\bullet+}$ was produced by reacting ABTS stock solution with a final concentration (2.45 mM) of potassium persulfate in the dark at room temperature overnight before use [50]. The solution was diluted until achieving absorbance at 734 nm of 0.7 (± 0.02), which corresponded to a final $ABTS^{\bullet+}$ concentration of 35 μM measured at 415 nm, with a molar extinction coefficient $\varepsilon = 3.6 \times 10^4$ mol^{-1} L cm^{-1}. In a quartz cuvette, 30 μL of CLP solution was added to 3 mL of $ABTS^{\bullet+}$ solution and the absorbance was monitored at 734 nm under the same conditions as described for the DPPH• test.

For both methods, the efficient concentration of antioxidant molecules needed to reduce 50% of the initial DPPH• or $ABTS^{\bullet+}$ ($EC50_{sol}$) was determined from the respective curve and expressed in g lignin/mol R•.

2.5.2. Scavenging activity of lignin in cellulose-based films towards soluble radicals, R•

The soluble radical scavenging activity of CNC-lignin and CNF-lignin films was evaluated by measuring their reactivity towards both DPPH• and $ABTS^{\bullet+}$ stable free radicals according to a previous study [22]. Pieces with film masses ranging from 0.1 to 4 mg were cut and immersed in 3 mL absolute ethanol $DPPH^{\bullet}$ (60 μM) or water $ABTS^{\bullet+}$ (35 μM) in a quartz cuvette. The absorbance (515 nm for $DPPH^{\bullet}$ and 734 nm for $ABTS^{\bullet+}$) was measured until reaching a plateau vs a quartz cuvette without film to determine the $EC50_{film}$ expressed in g lignin/mol $R^{\bullet}$ as tests of lignin in solution. A similar measurement was carried out on pure cellulose films as a control. A comparison of $EC50_{sol}$ and $EC50_{film}$ was performed after the expression of both parameters in g lignin/mol $R^{\bullet}$. To distinguish between the free radical scavenging activity of lignin films to the lignin ethanol- or lignin water-extractable fractions, similar measurements were made towards $DPPH^{\bullet}$ or $ABTS^{\bullet+}$ after 360 min of infusion of film in absolute ethanol (3 mL) or water (3 mL), respectively, as in [22]. The supernatant was mixed with 30 μL of 60 μM $DPPH^{\bullet}$ or 35 μM $ABTS^{\bullet+}$, and the absorbance was measured until the plateau was reached against the respective blank. The scavenging activity of the residual film towards $DPPH^{\bullet}$ or $ABTS^{\bullet+}$ was evaluated as previously described. The percentage of antioxidant activity of lignin released in ethanol or water media was calculated at the steady-state achievement of each kinetic. All the experiments were carried out in duplicate.

2.6. Antibacterial activity

The antibacterial activity of cellulose-lignin films was evaluated against *Escherichia coli* (CIP 54–127) and *Staphylococcus aureus* (CIP 53–154). The overnight culture prepared in nutrient broth (37 °C, 150 rpm, 16 h) was diluted (10^8 CFU/mL) before aseptic transfer of 250 μL to petri dishes containing composite films (free film sections (5 mm × 5 mm) or supported coating film on quartz slides (3.1 cm^2)). The films were incubated at 37 °C for 1 to 3 h under static conditions. Similarly, empty petri dishes and CNC and CNF film sections without lignin were incubated with the same bacterial suspension at the same temperature and time and used as positive controls. In the particular case of CNF-based films, circular sections (3.1 cm^2) were used. At the end of the incubation period, the inhibitory effect was estimated by measuring the total viable cell count after plating 1 mL of the inoculum samples on plate count agar with serial dilutions from 10^{-1} to 10^{-8} (37 °C, 24 h). All tests were performed in triplicate on one-week-old films. Growth factor reduction is equivalent to the log reduction (Log R), and it was estimated using Eq. (2):

$$\text{Log R} = \text{Log [A]} - \text{Log [B]} \quad (2)$$

where "A" is the mean value of three bacterial concentrations without film and "B" is the mean value of three bacterial concentrations in contact with cellulose-lignin film after the same time of incubation. A Log R value of 1 is equivalent to a 10-fold reduction or a 90% reduction of the population. A Log R value of 4 is equivalent to a 10^4-fold reduction or a 99.99% reduction of the population.

3. Results and discussion

The antioxidant and antibacterial properties of alkaline lignin in cellulose-based films were investigated as a function of the molecular and supramolecular lignin structures and the process used for its incorporation into the cellulosic network. For that, two gradual scales were chosen (Fig. 1). The first one was based on the molecular weight and/or the structural-morphology state of lignin before its use: monomer-dimer of lignin (CA), raw lignin sample solubilized in ethanol/water (6/4, v/v) solvent, two fractions of PB1000 treated by ionic liquid and solubilized in dioxane/water (9/1, v/v), or spherical CLP dispersed in water (Table 1). The second scale was established by the organization degree of the film brought by using two different nanocelluloses (CNC and CNF), which implies a variation in film thickness.

3.1. Characteristics of PB1000 and its different derivatives

PB1000 is composed of 50% guaiacyl (G) units, 49% syringyl (S) units and 1% *p*-hydroxyphenyl (H) units (in moles) with low contents of *p*-coumaric and ferulic acids (~0.5 wt%) [23]. These G, S and H units are mainly linked through resistant carbon-carbon bonds (5–5, β-5, β-β) and contain a small proportion of units only linked by aryl-aryl ether bonds (β-O-4), as indicated by its thioacidolysis yield of 83 μmol g^{-1}, which is ten times lower than that of native grass lignins. According to its apparent average molar mass (Mw), the average polymerization degree of PB1000 was estimated to be 6.4, assuming 196 g mol^{-1} as the mean unit molar mass value of lignin calculated from its empirical formula (Table 1) [51]. The free phenolic group content (2.7 mmol g^{-1}) was similar to that of other technical lignins [17] and consistent with the low content of (β-O-4) linkages. The water-soluble fraction (less than 2%, *w*/w) was composed of *p*-OH benzoic and *p*-coumaric acid, *p*-OH syringaldehyde and dimers/trimers of S and G units (data not shown).

The two fractions F1CH40 and F2CH40 produced by the IL treatment of PB1000 were previously characterized [23]. They showed the same molar mass distributions (Mn 676–680 g mol^{-1} and Mw 872–876 g mol^{-1}) and corresponded on average to tetra- or pentamers. F1CH40 and F2CH40 were both typified by enrichment in free phenols (6.6 and 8.3 mol g^{-1}, respectively) (Table 1). Moreover, they both contained phenolic monomers, mainly acidolysis ketones and acetosyringone that was demethylated once or twice [23]. These two fractions provided tools to assess the influence of lignin phenol content on the system.

CLP prepared from PB1000 had a very low polydispersity index (<0.15) and an average hydrodynamic diameter of 114.7 ± 5.2 nm.

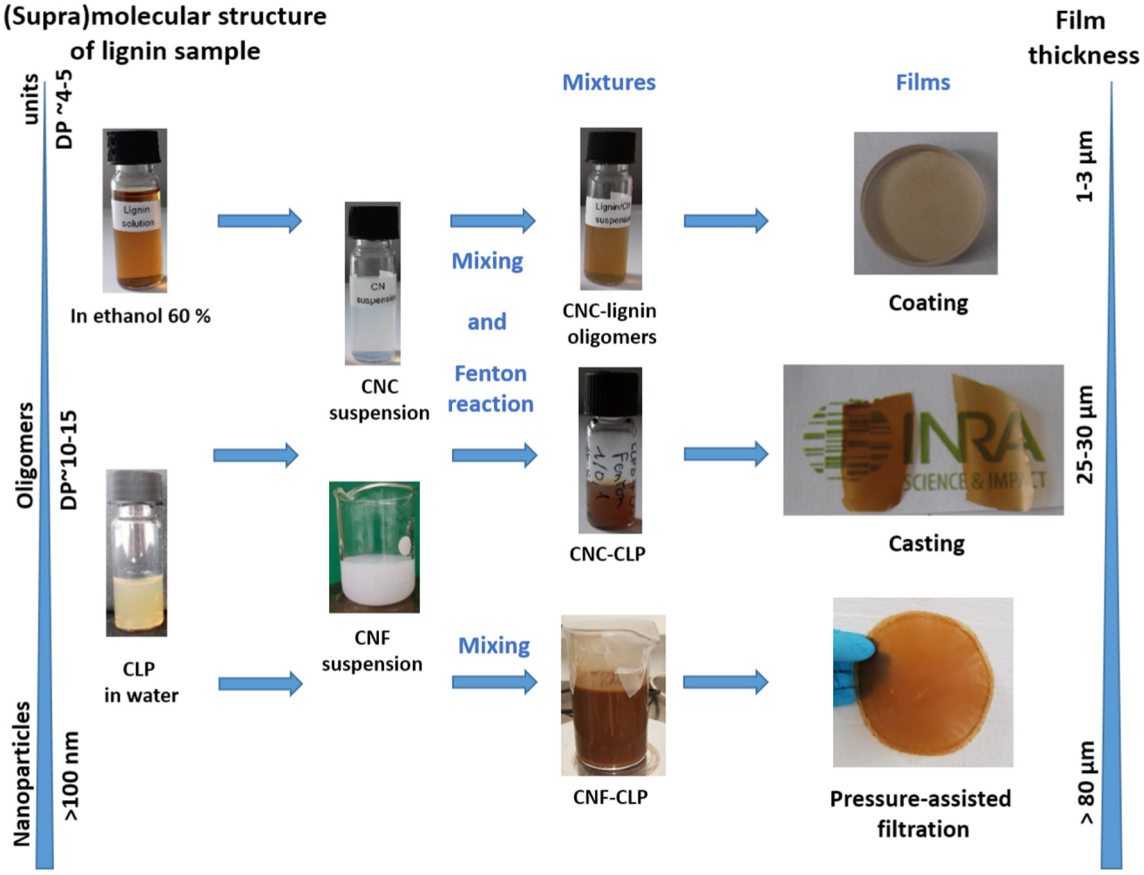

Fig. 1. Strategies to prepare cellulose-lignin-based films: mild chemical oxidation with Fenton reagent or filtration and hot drying pressure procedures using various phenolic structures ranging from oligomers to nanoparticles consisting of multiple oligomers. Images of coating and casting CNC films with 17 wt% PB1000 or CLP and CNF film with 10 wt% CLP.

They were easily dispersed in water to form stable aqueous suspensions as such or in the presence of cellulose nanocrystals because of their negative ζ potentials of −28.2 ± 4.3 mV and −50.1 ± 0.9 mV for CLP and CNC, respectively, in water. The CLP were used to assess the influence of the PB1000 supramolecular organization on the functionality of the composites. Indeed, since the CLP recovery yield exceeded 85%, it could be assumed that the chemical composition of CLP was representative of the initial PB1000 sample except for the possible loss of the water-soluble fraction. Table 1 summarizes the lignin sample characteristics, solvent conditions and cellulose nanoparticle type used for preparing the films and performing radical scavenging tests in solutions or in cellulose films.

3.2. Characteristics of uniform and stable lignin-cellulose suspensions before film preparation

A previous study demonstrated the possibility of grafting dehydropolymers (DHPs) and organosolv lignin oligomers onto CNC by mild chemical oxidation with Fenton's reagent in aqueous dioxane solvent [22,30] or by *in situ* polymerization of aromatic precursors of lignin (coniferyl alcohol) in water [39,47]. These treatments conferred new properties to the cellulosic materials, such as UV protection and transparency, antioxidant properties, and stable organic radical polymers (ORPs) [22,39]. A similar procedure was applied here to suspensions containing PB1000 or its derivatives using appropriate solvents (Table 1). The addition of Fenton's reagent to CNC-lignin mixtures containing 10 or 17 wt% lignin led to the formation of colloidal suspensions that were stable at room temperature for several months (Fig. 1, photographs). Indeed, lignin oligomers were previously shown to form nodular structures when the monomers were drop-by-drop polymerized in water or in aqueous solution of xylan [52] or upon self-assembly when water was added into THF/lignin solution [53]. The uniform yellow colour of all the CNC-lignin suspensions and the lack of precipitation demonstrated the colloidal stability of each system after chemical oxidative reaction and suggested a homogeneous distribution of aromatic molecules or nanoparticles onto the cellulose nanorods or fibrils. Both chemical oxidation before the evaporation step and physical mixing before the pressure-assisted filtration processes led to composite films with good washing resistance. This finding suggested good cohesion between lignin and CNC or CNF surfaces, either through noncovalent interactions, such as hydrogen bonds and hydrophobic interactions, or through covalent grafting via oxidation, which is consistent with previous studies [22,32].

3.3. Nanoscale surface morphology of cellulose-lignin films

The surface morphology at the nanoscale of the different films was analyzed by AFM. The AFM images provided three-dimensional information, including the surface roughness values of the films. AFM images representative of each CNC-based film at 45% RH are depicted in Fig. 2. CNC-F1CH40 and CNC-F2CH40 films (Fig. 2A and B) showed topography images (5 µm × 5 µm) with roughness (Ra) varying from 10 to 37 nm. CNC rods with a mean length value of 180.9 ± 12.5 nm [54] are not well distinguished due to the embedding phenomena by phenolic molecules more or less modified during the oxidative reaction. Only a few nodules could also be observed, linked perhaps to their higher phenol content (Table 1), which favours the interaction of these lignin derivatives with cellulose by hydrogen bonds. The AFM image of the CNC-PB1000 film showed on the contrary high amounts of nodules on the cellulose matrix with mean diameters of 383.6 nm ± 76.2 nm (Fig. 2C

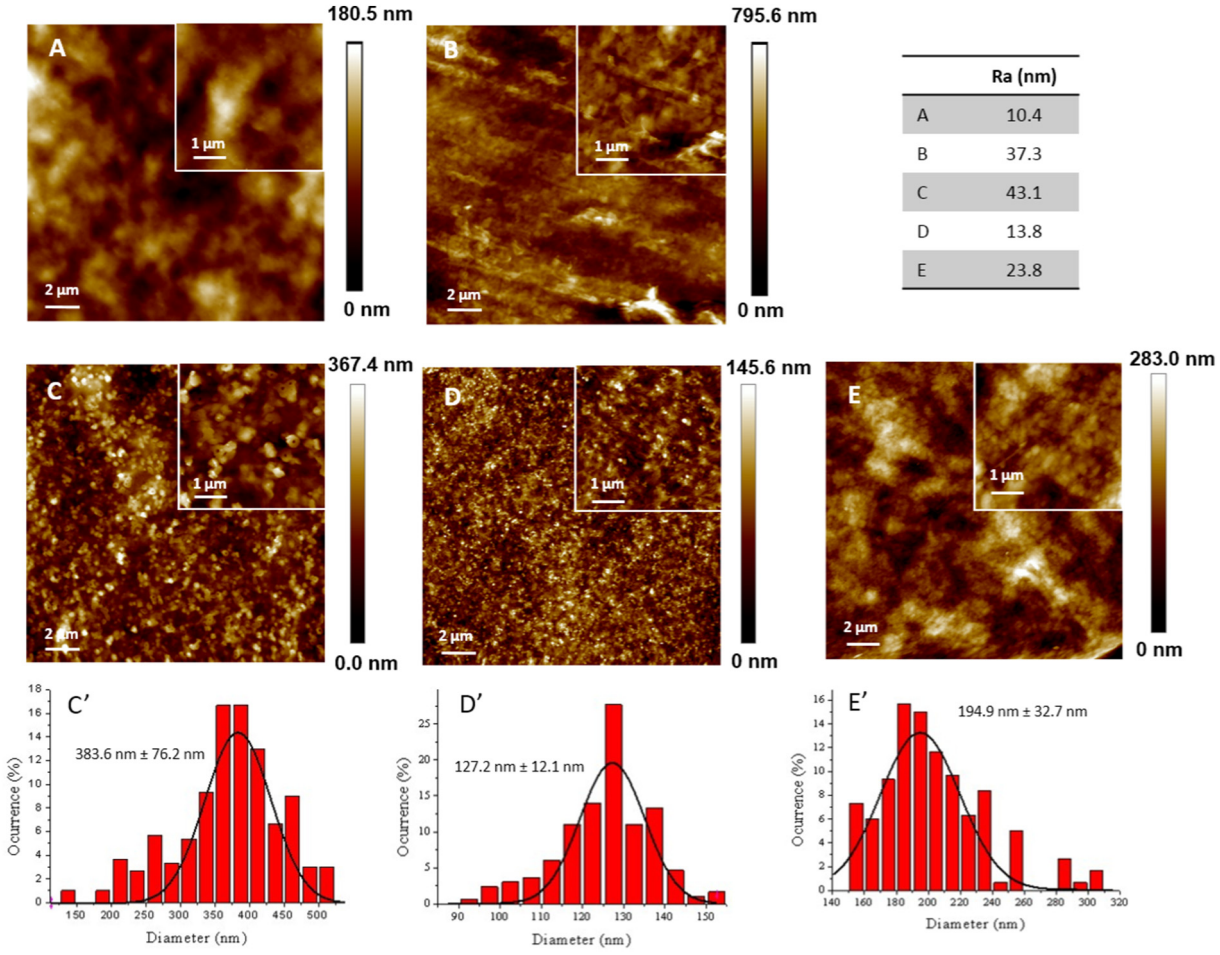

	Ra (nm)
A	10.4
B	37.3
C	43.1
D	13.8
E	23.8

Fig. 2. AFM topography analysis and size distribution of lignin nanoparticles in cellulose-based films. (A) CNC-F1CH40, (B) CNC-F2CH40, (C) CNC-PB1000, (D) CNC-CLP, and (E) CNF-CLP. Scan sizes for all AFM images are 20 µm × 20 µm. The inset figures represent zoomed images of 5 µm × 5 µm. Size distribution of lignin nanoparticles in CNC-PB1000 (D'), CNC-CLP(E') and CNF-CLP(F') (N = 300).

and C'). The Ra roughness of approximately 43 nm observed for the 5 µm × 5 µm image was higher than that observed for the other samples. These globular structures have been previously observed after oxidation of coniferyl alcohol and lignin oligomers with Fenton's reagent [31,39]. They are most often randomly distributed throughout the film, and their formation seems to be initiated in the aqueous suspension in contact with hydrophilic and hydrophobic faces of cellulose nanocrystal rods under moderate stirring, and they tend to grow in size during the drying step. Some nodules display "donuts" or an annular morphology (Fig. 2C') that is similar to the morphology observed with spray drying of CNC suspensions by hydrophobic lignin [55] or in organometallic nanocomposites based on zinc or iron oxides [56,57]. According to these previous works, the appearance of "donuts" could be explained by the hydrophobicity of lignin, which increases with the water evaporation kinetics during the drying step of the film. This process could cause a higher concentration of lignin in the nanoparticle centre with local high hydrophobicity due to the local faster evaporation of water than that on the surface of the crystalline faces of CNC. The presence of metal ions, such as Fe^{2+} and Fe^{3+} from Fenton's reagent, can also coordinate strong interactions between lignin and the surface of CNC, such as van der Waals bonds and hydrogen bonds, and induce particular assembly in the form of donut-like structures. The size distribution of these annular structures could also depend on the rate of water addition to the lignin solution, and it was inversely associated with the rate of addition of lignin solution to an excess of water [53]. Finally, according to the AFM image analysis, the CNC-CLP films showed a uniform distribution of nodules without donut-like structures, and they had a diameter range between 100 nm and 150 nm and a mean value of 127.2 nm ± 12.1 nm, which was close to that measured for the CLP suspension in water by DLS 110.8 nm ± 0.7 nm (Fig. 2D and D', SI1). The roughness of the CNC-CLP film was 14 nm ± 1 nm and lower than that of the CNC-PB1000 films. Thus, the mild oxidative reaction with Fenton's reagent in the CNC suspension did not significantly modify the CLP morphology. In addition, the CLP supramolecular structure appeared to be preserved in the CNF matrix, which is consistent with a previous study [58]. The structure was even preserved after a pressure-assisted filtration process, and the mean diameter was 194.9 nm ± 32.7 nm and the roughness was 24 nm (Fig. 2E and E'). For both studies, the lignin nanoparticles seem to be uniformly adsorbed on the CNF surfaces. The higher roughness values of the CNF-based films measured in our study can be explained by the use of native CNF without chemical surface modifications and lignin nanoparticles with a 2-fold to 5-fold higher mean size (CLP, 114 nm ± 5.2 nm) instead of TEMPO-oxidized CNF mixed with lignin nanoparticles prepared from mixed and prehydrolysed hardwood (nanoparticle sizes 10–50 nm). Thus, the CLP does not entirely penetrate the nanofibril network during the process.

3.4. Assessment of water accessibility of the films

The water sorption isotherms of cellulose-lignin films obtained by dynamic vapor sorption (DVS) measurements were used to perform an indirect assessment of the intramolecular voids left between lignin nodules and cellulose nanorods or nanofibrils. These voids can form

nano- or microcavities that are accessible by water molecules (Fig. 3). Both the oxidative treatment and the pressure-assisted filtration process induced some linkages between lignin and the CNC surface, thus increasing the water retention capacity of the films compared to the initial nontreated CNC and CNF films [22,32]. All samples exhibited sigmoidal curves during water sorption and desorption in a 10–90% relative humidity range. This phenomenon, called hysteresis, was previously observed and followed a similar trend [22,32], and it is associated with the deformation of the films induced after swelling during the water sorption steps. For the films composed of raw PB1000 and CLP, the water content increased until approximately 25% when the RH increased from 10 to 90% by the formation of water sorption sites on the surface of the polymer chain intertwined inside the film (represented by the A_L factor between 0 and 20% RH), the linear sorption of water (represented by K_H between 20 and 60%) and finally the formation of water molecule aggregates (represented by K_a and n) according to the Park model (Fig. 3, Table insert). No significant differences were observed between the Park parameter values for both PB1000 and CLP incorporated at 10 wt% in CNC-based films, except for CLP mixed with cellulose nanofibrils, where A_L was the highest value (0.10 $g_{water} \cdot g^{-1}_{dry\ matter}$) of the film range and K_a was the lowest (0.25 $g_{water} \cdot g^{-1}_{dry\ matter}$), with a n value of 9.5. This observation suggested that the nucleation sites of water aggregates in the CNF-based film prepared by the pressure-assisted filtration process were smaller than those in films prepared by oxidation with Fenton's reagent. In the same manner, the hysteresis profile (D—S,%) showed that water molecules at RH < 20% and water aggregates at RH > 60% could be trapped in the network, even after several hours of desorption, until an equilibrium state was reached, i.e., 0.5% and 2.5–3 % water content, respectively (Fig. 3A insert). In contrast, for F1CH40- and F2CH40-derived lignin, the water content in the RH range at the end of the isotherm (RH > 60%) was higher than the water content of PB1000-containing films and then increased to reach the highest values for the K_a and n parameters (0.43 $g_{water} \cdot g^{-1}_{dry\ matter}$ for F1CH40 and F2CH40, with n values of approximately 9.8 and 10.1, respectively (Fig. 3B)). This result suggested that the number and/or size of the water aggregates increased for these samples and were less easily desorbed from the network during the desorption step in comparison with PB1000 (Fig. 3B insert). These phenomena could be explained by the increased content of phenolic groups, which are more likely to interact with the hydroxyl groups of cellulose via hydrogen bonds, and the sorption of water molecules, which can become the nucleation sites of water aggregates trapped inside the network at high RH. In conclusion, all Park parameter values indicated that the affinity of cellulose-lignin films towards water molecules and their capacity to trap water aggregates were dependent not only on the polymerization degree of the lignin oligomer but also on the phenolic group content. This dependency could be explained by the influence of both parameters on the formation of nodular structures of various sizes embedded in the cellulose matrix. To better understand the chemical structure of all films, FTIR measurements were performed on the same samples to identify variations in functional groups before and after oxidative or physical film processing.

3.5. Influence of film processing on lignin functional groups

FTIR analysis of the isolated lignin samples before film preparation (Fig. 4A) indicated that PB1000 and CLP had similar spectra, thus confirming that CLP retained the main structural characteristics of PB1000. The bands at 1708 cm^{-1} and 1215 cm^{-1} were assigned respectively to conjugated aldehydes and carboxylic acids (C═O) and to aryl-ether groups (C—O); the bands at 1600, 1515, 1425 and 1269 cm^{-1} were assigned to aromatic skeleton vibrations; the band at 1462 cm^{-1} was assigned to C—H stretching in the $-CH_3$ and $-CH_2-$ groups; and the bands at 1115 and 1032 cm^{-1} were assigned to C═O stretching vibrations and aromatic CH- in plane deformation, respectively [59,60]. The only differences between PB1000 and CLP occurred in the intensity decrease of the bands at 1328 cm^{-1} (C—O deformation in syringyl units), 1515 cm^{-1} and 1608 cm^{-1} (aromatic skeleton) and the disappearance of the band at 1315 cm^{-1} (CH_2 rocking/wagging). These differences were consistent with the location of such apolar structures in the core of the nanoparticles, which is consistent with previous NMR analyses [61]. The spectra of the two fractions F1CH40 and F2CH40 showed major differences with PB1000 and CLP [26,60,62]: increased intensity of the OH stretching bands between 3100 and 3300 cm^{-1} and decreased intensity at 1708 cm^{-1} (C═O ester groups), at 1515 and 1425 cm^{-1}relative to the aromatic ring bonds), at 2915 cm^{-1} and 1460 cm^{-1} relative to the C—H stretching in the methoxy groups and at 1325 cm^{-1}, which corresponded to the resonance of the C—O stretching of the S units [26]. The absorption maxima of the ether bond band at 1211 cm^{-1} for PB1000 and CLP shifted to lower wavenumbers at 1200 cm^{-1} associated with phenolic OH deformation for the two derivatives (Fig. 4A). These differences are fully consistent

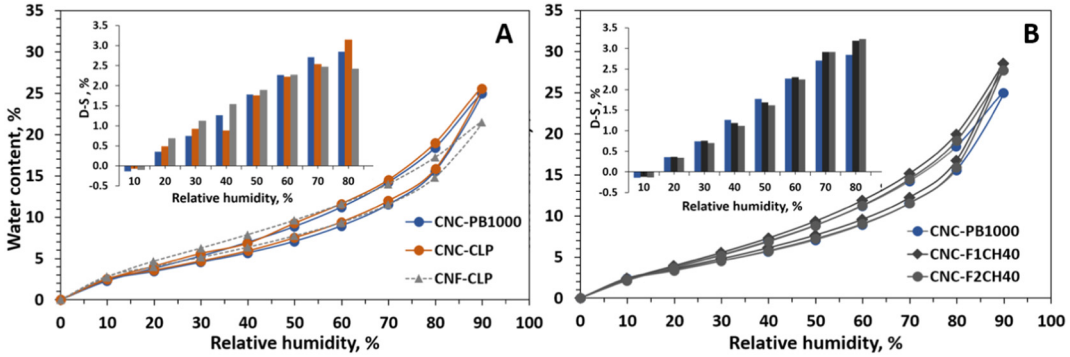

Films(10%)	$A_L \times 10^{-1}$	K_H	K_a	n
	$g_{water} \cdot g^{-1}_{dry\ matter}$			
CNC-PB1000	0.05	0.13	0.31	8.6
CNC-CLP	0.05	0.14	0.33	9.4
CNF-CLP	0.10	0.14	0.25	9.5

Films(10%)	$A_L \times 10^{-1}$	K_H	K_a	n
	$g_{water} \cdot g^{-1}_{dry\ matter}$			
CNC-PB1000	0.05	0.13	0.31	8.6
CNC-F1CH40	0.04	0.15	0.42	9.8
CNC-F2CH40	0.04	0.14	0.43	10.1

Fig. 3. Water sorption isotherms and hysteresis (D—S, % insert) of CNC- and CNF-based films with 10 wt% lignin. (A) Data comparison for PB1000 and CLP in CNC and CNF films. (B) Data comparison for PB1000 and derivatives after IL treatment (F1CH40 and F2CH40) in CNC films. D, desorption data; S, sorption data. Tables: respective Park parameters calculated by fitting the Park equation described in [47]. The calculated deviation modulus E is inferior to 2%.

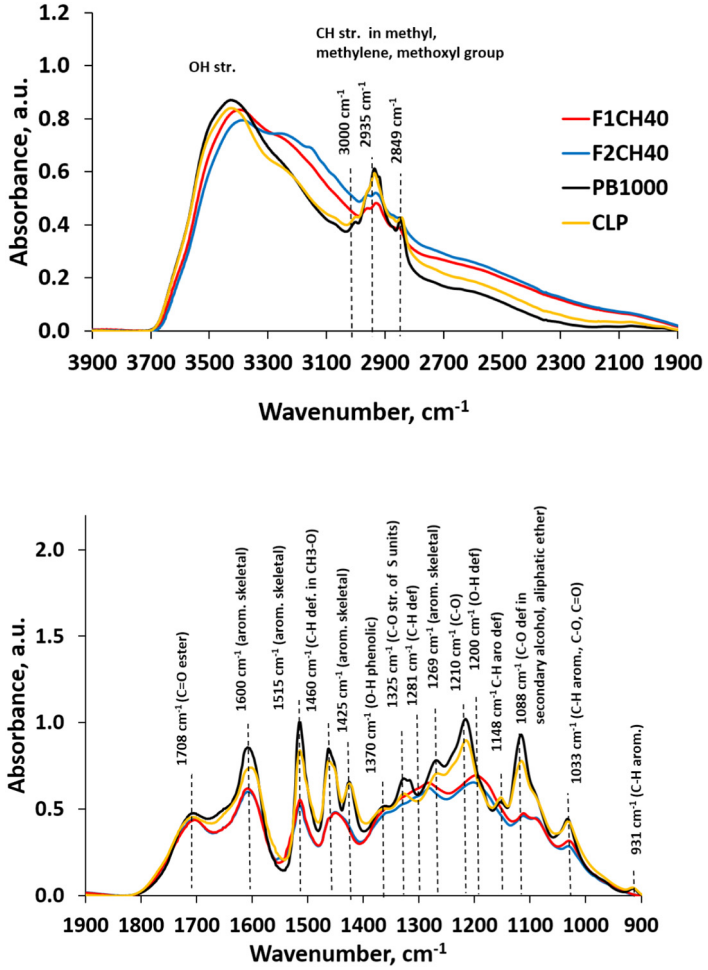

Fig. 4A. FTIR spectra of raw and derived PB1000 lignin samples. The vertical lines indicate the specific bands of lignin oligomers.

with the fact that EA fractions of PB1000 after [HMIM]Br treatment arose from the cleavage of ether bonds and yielded additional free phenols in all the fractions (F1CH40 and F2CH40, Table 1) because of depolymerization and demethylation [23].

After their respective introduction in CNC-based films, the PB1000 and CLP spectra maintained their main characteristic bands without any variation (Fig. 4B), except for the shifting of the band at 1708 cm^{-1} to 1716 cm^{-1} (C═O stretching in unconjugated ketones, carbonyls and esters), which was caused by oxidation with the Fenton's reagent, and the band at 1515 cm^{-1}, which was related to the vibration of aromatic rings. The intensity of the band at 1716 cm^{-1} increased for F1CH40 and F2CH40, and the intensity of the band at 1515 cm^{-1}

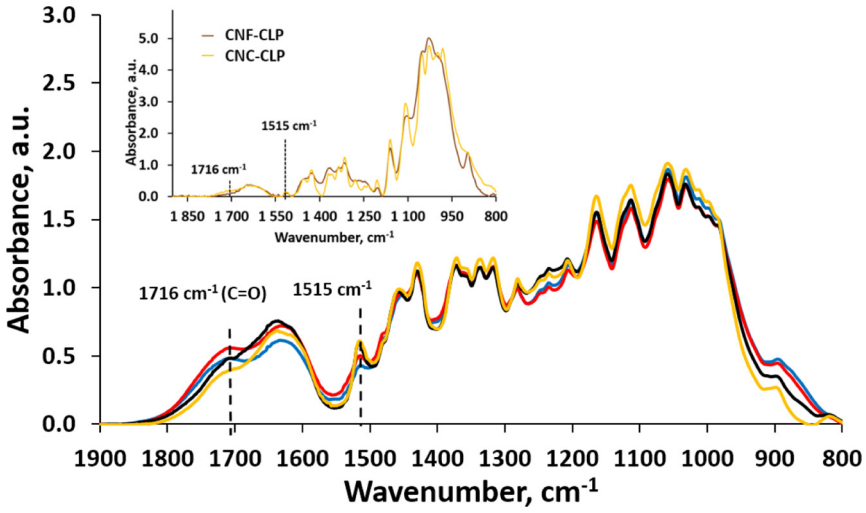

Fig. 4B. FTIR spectra of raw and derived PB1000 lignin samples in CNC-based films with 17 wt% lignin content and measured on KBr tablets. Insert: IR spectra of CNF-CLP film in comparison with CNC-CLP film with 10 wt% lignin content and measured by Attenuated Total Reflectance.

decreased in comparison with the same bands observed in the PB1000 and CLP spectra. The ratio between the intensity (I) of these two bands I_{1716}/I_{1515} was higher for F1CH40 and F2CH40 than for PB1000 and CLP in the CNC-based films (1.1 and 0.7, respectively). This finding could explain the slight generation of phenolic esters or ketones after oxidative reaction using Fenton's reagent for these two PB1000 derivatives with a higher content of phenolic groups after the combined process (Table 1). Nevertheless, the F1CH40 and F2CH40 spectra were similar to those of the PB1000 and CLP-based films between 1060 and 950 cm^{-1}, suggesting that IR absorption was mainly governed by the cellulose network characterized by these bands (Fig. 4B). This last result was even more apparent with the CNF-based film prepared by pressure-assisted filtration and drying at ambient temperature (Fig. 4B insert). Furthermore, no additional band was observed at 1740 cm^{-1}, which is inconsistent with previous studies that used higher concentrations of hydrogen peroxide [30,39] or peroxidase [47].

3.6. Influence of lignin molecular and supramolecular structures on the radical scavenging capacity (RSC) of the material

To assess the influence of molecular and supramolecular structures of lignin on their radical scavenging properties and thus their antioxidant potential, RSC measurements were performed on three types of systems with increasing organization level: isolated lignin in solution, CLP aqueous suspension, and lignin in cellulosic solid films.

3.6.1. RSC in solution/suspension without cellulose

The radical scavenging capacity (RSC) of all lignin samples was tested towards DPPH$^{\bullet}$ and $ABTS^{\bullet+}$ in absolute ethanol and water without cellulose by measuring the $EC50_{sol}$ parameter, which is defined as the antioxidant concentration required to reduce 50% of the initial free radicals [22]. This parameter was determined from Fig. 5 and represents the percentage of radical species reduced versus the lignin content in solution (Fig. 5A) or in film (Fig. 5B) per molar content of free radicals ($R^{\bullet}$) in medium (absolute ethanol for DPPH$^{\bullet}$ and water for $ABTS^{\bullet+}$). A larger $EC50_{sol}$ value corresponds to a lower RSC. PB1000 solubilized in aqueous organic solvent (ethanol/water (6/4, v/v)) showed a similar RSC towards DPPH$^{\bullet}$ as CLP dispersed in water, and it had an average $EC50_{sol}$ value of 0.87 ± 0.08 g of lignin per mole of DPPH$^{\bullet}$ (corresponding to lignin bulk concentration of 0.33 ± 0.03 g L^{-1}). The nanoparticle structure of CLP is not stable in absolute ethanol solution and loses its nodular structure; thus, similar $EC50_{sol}$ values were obtained for CLP and raw PB1000, which could be explained by the recovery of the initial dissolved state after dilution of CLP in the ethanolic solution implemented for the test (Fig. 5A). This finding also demonstrates that the PB1000 oligomers were not chemically modified during the preparation of CLP. To avoid this effect of dissolution, tests were also performed for $ABTS^{\bullet+}$ in water, wherein the CLP structure was preserved. Both PB1000 and CLP showed lower $EC50_{sol}$ values than the DPPH$^{\bullet}$ tests, and this finding reflected the more efficient scavenging process in aqueous $ABTS^{\bullet+}$ than in ethanolic DPPH$^{\bullet}$ solutions. This increased efficiency was less pronounced for CLP than for PB1000 (0.48 ± 0.04 g mol^{-1} for CLP and 0.36 ± 0.04 g mol^{-1} for PB1000), suggesting that the organization into nanoparticles limited the access of the radicals to some phenol groups. This limited access could be explained by the presence of phenol groups in the core of the particles (25%, according to the $EC50_{sol}$ difference between PB1000 and CLP systems) and/or to the possible steric factors that control the reactions [63]. Indeed, the reaction becomes impeded as the structural complexity and size of the molecule increases due to the additional rings that interfere with access to $ABTS^{\bullet+}$ and greater number of DPPH$^{\bullet}$ sites that are landlocked between two benzene rings (Fig. 5A insert). Nevertheless, most of the RSC of PB1000 was preserved, even after self-assembly into CLP. F1CH40 and F2CH40 were previously shown to have antioxidant properties that compete with coniferyl alcohol, ferulic acid and BHT in solution towards DPPH$^{\bullet}$ [23]. These fractions were not suitable for the $ABTS^{\bullet+}$ test due to their tendency to aggregate in total aqueous solution. Thus, consistent with their 2- to 3-fold higher phenol group contents, these fractions exhibited a 3-fold lower $EC50_{sol}$, which was determined through the DPPH$^{\bullet}$ tests (0.30 ± 0.01 g mol^{-1} corresponding to a lignin bulk concentration of 0.11 ± 0.005 g L^{-1}).

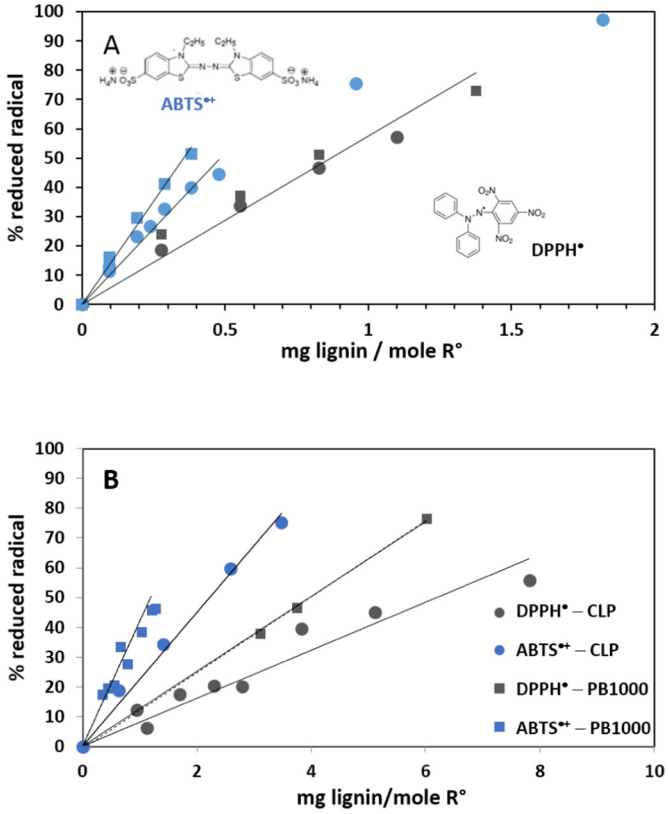

Fig. 5. Antioxidant properties of raw and derived PB1000 in solution (A) and in CNC-based films (B) towards DPPH$^{\bullet}$ and $ABTS^{\bullet+}$.

3.6.2. RSC in cellulosic film

The RSC towards DPPH$^{\bullet}$ and $ABTS^{\bullet+}$ were measured for all CNC-lignin films, and the corresponding $EC50_{film}$ (efficient lignin concentration in film required to reduce 50% of the radicals) was calculated (Fig. 5B). This parameter was measured by selecting the film mass range (g) to obtain a linear relation between the percentage of reduced radicals and the ratio g lignin/mol. $R^{\bullet}$. Since no antioxidant properties of pure CNC or CNF film could be detected, these $EC50_{film}$ values were compared with the $EC50_{sol}$ values for each lignin sample (Fig. 5A) to assess the influence of the process of incorporating lignin into the film. Moreover, the RSC of the films was related to the presence of phenol groups, either in the film or at the surface of the material or carried by phenolic compounds released in the radical solution during the test [22]. As for $EC50_{sol}$, the $EC50_{film}$ values varied according to the structure of the lignin samples and were lower with the aqueous $ABTS^{\bullet+}$ solution than with ethanolic DPPH$^{\bullet}$ solution. Thus, for the CNC-PB1000 film, the $EC50_{film}$ value was 3-fold lower for $ABTS^{\bullet+}$ than DPPH$^{\bullet}$ (1.21 ± 0.04 versus 3.98 ± 0.05 g mol^{-1}) and 2.5-fold lower for the CNC-CLP film (2.22 ± 0.04 versus 6.19 ± 0.05 g mol^{-1}). Expressed in mg of tannic acid equivalent (TAE), the RSC of the CNF-CLP film was equal to 0.6 ± 0.1 mg TAE per g of film, as indicated in a previous study [32] (or 6.4 ± 0.7 mg TAE per g lignin in film) (Table S1). The corresponding values for CNC-CLP and CNC-FA01 were 3.6 ± 0.2 mg and 6.4 ± 0.4 mg TAE per g of film respectively. Interestingly, the better performance of PB1000 compared to CLP was retained after incorporation in the film, indicating that the nanostructure of CLP was preserved within the cellulosic film. However, film processing led to a lower RSC for both samples, with a

reduction from 3.4 (for $ABTS^{\bullet+}$) to 4.4 (for $DPPH^{\bullet}$) times for PB1000 and from 5.0 (for $ABTS^{\bullet+}$) to 6.8 (for $DPPH^{\bullet}$) times for CLP. These results suggested a lower accessibility of the radicals to the phenol groups as a consequence of their embedding in the cellulose matrix and limited extractability (Fig. 6 and table insert: 22% antioxidant activity in film against 78% antioxidant activity released in water after 6 h of immersion of CNC-PB1000 film and 37% and 63% for CNC-CLP, respectively). This phenomenon was more pronounced when the lignin samples were introduced into the CNF film by blending prior to high-pressure filtration and drying at room temperature (CNF-CLP, 10 wt%). Indeed, in that case, no radical scavenging was detected towards $DPPH^{\bullet}$ in ethanolic solution and the $EC50_{film}$ for $ABTS^{\bullet+}$ in aqueous solution was 4 times higher than the activity of CNC-CLP, with an identical rate of release after immersion in water (40% antioxidant activity in film against 60% released in water) (Fig. 6 insert). This different behaviour of CNF-CLP towards $DPPH^{\bullet}$ and $ABTS^{\bullet+}$ was probably due to the lower swelling of the film in ethanol compared to that in water. Greater swelling of the films could enable better penetration of the reagents into the film. Thus, all films prepared by the oxidative procedure showed higher RSC than films prepared by filtration and hot pressing process, which suggested that phenolic compounds were less accessible with this last process. The difference by a factor approximately 4 in the $ABTS^{\bullet+}$ test between the CNF-CLP and CNC-CLP films could also be explained by the difference of film area in contact with water (84.8 mm^2 (corresponding to approximately 2.6 mg of film) for CNF-CLP 10 wt% and 17.5 mm^2 corresponding to approximately 0.7 mg of film) for CNC-CLP 10 wt%, (Table S1). Taken together, these results showed that both the film preparation and the test influenced the RSC of the films, with maximal performance observed for $ABTS^{\bullet+}$ in aqueous solution. Moreover, they showed that the CLP structure was preserved in the film, which decreased the accessibility of some of the phenol groups to the surrounding medium. Despite these results, the free remaining portion of lignin in the nanocomposite film was able to trap free radicals in the medium (more in water than in ethanol) that were in contact with the material and remains an active additive for the oxygen barrier properties, which are observed in well-known cellulosic materials for packaging [64].

To further assess the influence of the lignin chemical structure on the RSC of the films, F1CH40 and F2CH40 were incorporated in the CNC film at 10 wt% by a mild oxidative process for comparison with PB1000 and CLP (Fig. 6). Whereas PB1000 supramolecular organization into CLP led to reduced RSC values, particularly after film formation, its conversion into phenol-rich oligomers (F1CH40 and F2CH40) led to enhanced RSC values, notably for $DPPH^{\bullet}$, thus leading to the following RSC-decreasing order of F1CH40 ≥ F2CH40 ≫ PB1000 ≫ CLP. As for PB1000 and CLP, incorporation of the phenol-rich fractions in the cellulosic films decreased their RSC measured in solution (3-fold increase in $EC50_{sol}$). However, their $EC50_{film}$ value was still 4.5-fold lower than that of unmodified PB1000-based films. In addition to their initial higher phenol group content, the lower molar mass could explain the good performance in the films. Indeed, the lower molar mass favoured both a higher miscibility with the matrix and partial release into the medium [22]. Moreover, topographic images of the films showed fewer nodules for films containing F1CH40 or F2CH40 than for those containing PB1000 and CLP (Fig. 2). This lower level of supramolecular organization would account for the higher accessibility of phenol groups.

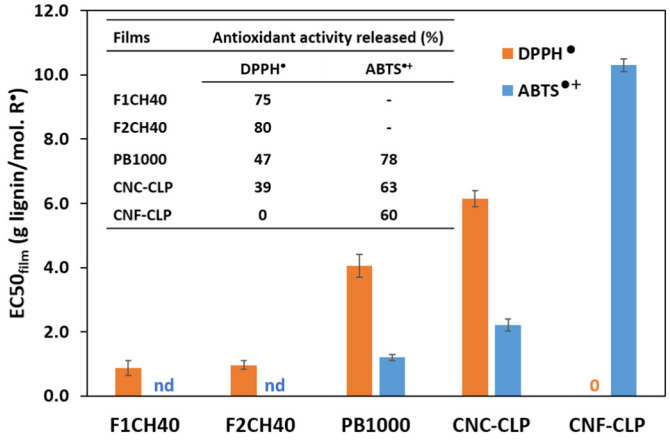

Fig. 6. $EC50_{film}$ values (g lignin. mol^{-1} $R^{\bullet}$) of all cellulose-based films (CNC and CNF) and antioxidant activity released after 6 h of immersion in the respective stable ethanolic $DPPH^{\bullet}$ and aqueous $ABTS^{\bullet+}$ solutions (insert). F1CH40, F2CH40, PB1000 and CNC-CLP films were prepared by chemical oxidation procedures. CNF-CLP was prepared by pressure-assisted filtration and drying at ambient temperature.

These results demonstrated that both the phenol group content and their accessibility to radicals control the radical scavenging performance of materials. The accessibility is higher when the phenol groups are located at the surface of the films and when the phenolic compounds are not assembled in particles or nodules in the matrix. Indeed, despite the presence of water-trapping cavities allowing penetration of aqueous solution into the film, the transfer of protons between free phenol groups and radical species requires the exposure of the phenols towards the surrounding medium. This conclusion was clearly supported by the absence of RSC towards $DPPH^{\bullet}$ in ethanolic solution for the CNF-CLP film. Even if soluble radicals are not reduced efficiently in the presence of nanoparticles, some radicals might be trapped by the particles and stabilized through aromatic ring interactions. Moreover, the RSC of the films might depend on the stabilization of the phenoxy radicals formed through $DPPH^{\bullet}$ or $ABTS^{\bullet+}$ reduction and/or after mild oxidative treatment with Fenton's reagent. Therefore, an investigation of the radical stability in the films using phenoxy radicals was undertaken.

3.7. Benefit of lignin structuration to maintain the antibacterial properties of cellulose-lignin films

To evaluate the antimicrobial properties of PB1000 in CNC-based films, an initial screening was carried out by performing inhibition tests in agar medium. These plate tests enabled us to qualitatively evaluate the properties of the films with regard to different bacterial species, namely, *E. coli*, *P. aeruginosa*, *S. aureus*, *B. subtilis*, and *E. hirae*. The films showed significant activity against *E. coli* and *S. aureus* as the main representative gram-negative and gram-positive bacteria, respectively, which are responsible for food poisoning, localized suppurative infections and, in extreme cases, potentially fatal infections (for the latter). Thus, no growth was visualized on the surface of the films and a slight inhibition zone was observed on the periphery of these films (data not shown). To quantify this antibacterial effect against these two bacteria, inhibition tests in liquid medium were carried out. For this purpose, CNC-PB1000 film sections of approximately 4 mg weight mass (i.e., 25 mm^2 of surface area) and from one week to a few months of age were incubated in the respective culture media (10^8 CFU/mL) with respect to the control. A bacterial viability reduction was not clearly observed against *E. coli* (Fig. S2). In contrast, after 1 and 3 h of contact with the CNC-PB1000 film, the growth factor reduction of *S. aureus* (Log R) reached 1.0 and 1.5 from 2.0 to 3.4 for the one-week- and four-month-old films, respectively. Similar contrasting antibacterial properties were observed for lignin-precipitated cellulose-lignin beads [65,66] and more recently for polyethylene blends [67]. Similar experiments were performed with PB1000 and CLP by using supported coating films on quartz slides with the objective of increasing the surface contact area (3.1 cm^2) with *S. aureus* culture media. Fig. 7 confirms the decreased growth of *S. aureus* for PB1000 in the CNC film, which had a Log R value between 0.3 and 0.4 after 1 and 3 h of incubation. The CLP seemed to be more efficient in the CNF film with higher Log R values (between 0.35 and 0.5), which was perhaps due to the high distribution of nanoparticles on the cellulosic film surface observed by AFM (Fig. 2D) and the film mass difference between the CNC-lignin film coated on the quartz slide (thickness on the order of 1.5 μm for the coated film and 80 μm for the CNF-lignin self-supported film). In

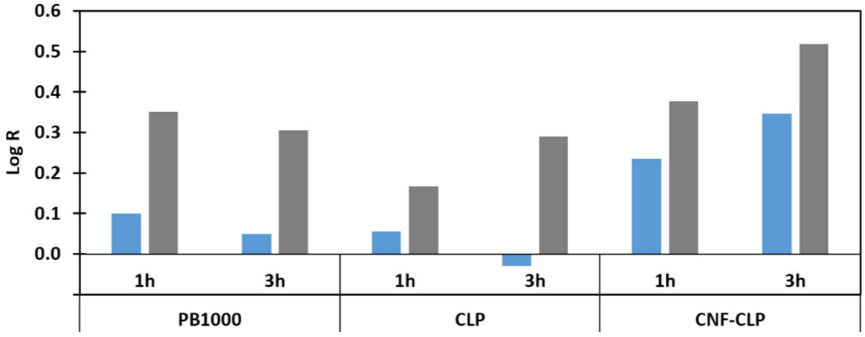

Fig. 7. Growth factor reduction (Log R) towards *Staphylococcus aureus* (gram$^+$) of PB1000 and CLP lignin samples incorporated in CNC- and CNF-based films at 17 wt% and 10 wt%, respectively (grey bars). Controls (blue bars) are the corresponding cellulose films without lignin.

comparison, the CNC and CNF control films showed a decrease in growth that did not exceed 0.1 and 0.35 after similar time periods, respectively. Thus, regardless of the formulation mode and the nodular structuration level of lignin oligomers, we confirmed that the lignin samples were effective against the gram-positive bacteria *S. aureus* but less effective against the gram-negative bacteria *E. coli*. According to previous studies, the antimicrobial activity of lignin is based on its interaction with the surface layer of bacteria composed of peptidoglycan [66]. Moreover, cellulose films prepared with mild oxidative processes show stable phenoxy radicals [39] that could influence antimicrobial activity as redox-active antimicrobial complexes based on diphenol due to their possible ability to affect the electron-transport chain on bacteria [68].

3.8. Benefit of lignin structuration with respect to phenoxy radical stabilization

The Fenton reaction involves reactive oxygen species (ROS) in mixtures of cellulose and lignin model compounds (LMCs), which turn phenols into phenoxy radicals [39]. The formation and evolution of persistent phenoxy radicals in cellulosic films were demonstrated by the proportional EPR signal to the $EC50_{sol}$ values and the apparent average molar mass of the LMC. To further elucidate the organization of phenols in CLP within cellulosic materials, an EPR analysis was performed on the CNC-CLP film under the conditions of an oxidative reaction process (1 mM $FeSO_4$/0.1 mM H_2O_2), and the results were compared to the CNC-PB1000 film (Fig. 8). EPR signals were observed at a g factor of 2.0030, which is consistent with that of phenoxy radicals as CNC-LMC films [39]. The amplitude signals, which are expressed per gram of lignin in the films, were proportional to the apparent polymerization degree considering the mean mass value of the phenylpropan unit ($C_9H_9O_2(OCH_3)_{1-2}$) of 196 g mol^{-1}, and they were inversely proportional to the phenol content (PhOH) values measured by ^{31}P NMR according to [22] (insert in Fig. 8). The comparison of the EPR data between PB1000 and CLP showed that oxidation by Fenton's reagent was responsible for the formation of phenoxy radicals in the films, with fewer radicals for PB1000 than for CLP (1988 10^6 a.u. g^{-1} film against 3195 10^6 a.u. g^{-1} film). The empirical content value of the phenolic units ($PhOH_{EPR}$, mmol g^{-1} lignin) converted into phenoxy radicals per CLP can be estimated from the relationship between the EPR signal amplitude (10^6 g^{-1} lignin) and total phenol content and was on the order of 0.77 mmol g^{-1} for the CNC-CLP film and 1.75 mmol g^{-1} for the CNC-PB1000 film. These values corresponded to 24% and 65% of the total PhOH content measured by ^{31}P NMR of raw PB1000 (Table 1 and Fig. 8 insert). This finding is consistent with the nodular structures observed in both CNC-based films (Fig. 2C and D) and suggests that some phenolic groups are not free but are either linked to cellulose by hydrogen bonds or oxidized during the preparation of the films, which can explain their loss of antioxidant power (Fig. 6). Nevertheless, this loss of antioxidant power of CLP can favour another functionality, such as the capacity to trap stable organic radicals in composites, which could be useful for electronic applications. Moreover, the EPR results can also be used to estimate a rough amount of PB1000 oligomer moles constitutive of one CLP as follows. Considering that one CLP would be composed of n moles of initial PB1000 oligomer (n times 7 monomer units) with a respective total phenol content of 2.7 mmol g^{-1}, the theoretical EPR signal should be equal to 3195 10^6 a.u. g^{-1} lignin multiplied by the ratio $PhOH_{PB1000}/PhOH_{EPR}$ (= 2.70/0.77 for CNC-CLP) (Fig. SI3). This new empirical EPR signal would then correspond to the theoretical number of monomer units for one CLP (with a mean size value of 114.7 ± 5.2 nm) on the order of 75 monomer units according to the relation between the EPR signal amplitude (10^{-6} g^{-1} lignin) and monomer unit number (Pd, polymerization degree) of LMC (Fig. SI3). This unit number corresponds to a mean of eleven oligomeric PB1000 moles per CLP (Table 1). In conclusion, some phenolic groups of CLP can be converted into persistent phenoxy radicals. These groups are oriented towards the outside of the nanoparticle. However, most of them seem to be either localized in the core of the nanoparticle or linked to cellulose by hydrogen bonds in the composite film.

4. Conclusions

In this study, the diversity of lignin structural levels was successfully exploited to determine the relationships between lignin functional group accessibility, cellulose-lignin composite morphologies and lignin functional properties in the different systems. The nodular organization of lignin compounds in the cellulosic matrix was shown to be controlled by the amount of accessible phenolic groups in addition to the polymerization degree. They were shown to govern the capacity of the composites to trap water aggregates and accounted and to scavenge soluble radical species in ethanolic or aqueous solutions. Converting lignin into phenol-rich oligomers allowed to enhance the RSC while self-assembly into CLP reduced it, as a consequence of the lower accessibility of phenolic groups. However lignin structuration did not affect the antibacterial properties towards *S. aureus*. Thus, both CLP and lignin derivatives have the potential for use as active additives in cellulosic packaging materials. The capacity of CLP to trap stable phenoxy radicals in cellulose composites after oxidative treatment offers new perspectives for sensors and electronic applications.

Funding sources

This work was funded by the Bio Based Industry Joint Undertaking under the European Union's Horizon 2020 research and innovation programme within the Zelcor project (under the grant number No 720303), part of the COFILI project (grant number D201550245) for AFM measurements funded by the Grand Est Region and the European FEDER Programme and the Lignoxyl project for EPR measurements supported by the Agence Nationale de la Recherche (ANR) through the Carnot Institutes 3BCAR (www.3bcar.fr) and Qualiment (https://

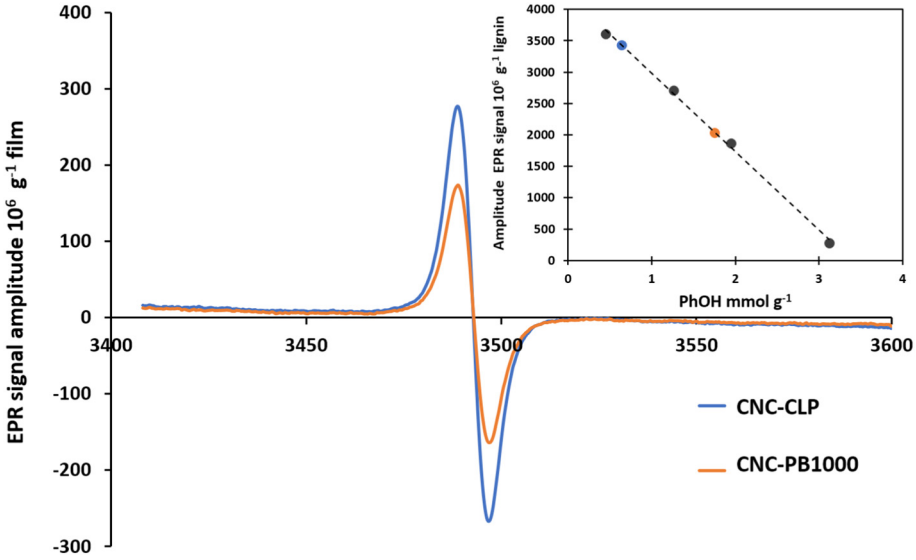

Fig. 8. X-band EPR spectra of crushed films, CNC-PB1000 and CNC-CLP (17 wt% lignin content) prepared with Fenton's reagent (1 mM $FeSO_4$, 0.1 mM H_2O_2, pH 3). Insert: Relationship between the phenol group content (PhOH, mmol g^{-1}) in LMC samples determined by ^{31}P NMR and the phenoxy radical signal amplitude per g of lignin in CNC-based film. (The linear equation was [EPR signal 10^6 g^{-1} lignin] = −1248.2 [PhOH mmol g^{-1}] + 4231, R^2: 0.9976).

qualiment.fr/) (no. 3 no. 19-CARN-001-01 and no. 16-CARN 001-01). The EPR data in this manuscript were obtained using equipment supported jointly by the French National Ministry of Research (PPF IRPE), the "Fondation pour la Recherche Médicale" (FRM DGE20061007745), and the CNRS (Department of Chemistry and Life Sciences). The IJPB benefits from the support of the LabEx Saclay Plant Sciences-SPS (ANR-10-LABX-552 0040-SPS).

CRediT authorship contribution statement

V.A—B., B.K., S.B. and M.Ö. conceived the scientific strategy of the study within the framework of the Zelcor project, which is coordinated by S.B. E.G. and Y.M.F. performed the EPR measurements and interpreted the experimental data. G.N.R., L.F., and B.G. conceived of the cellulose films and performed their spectroscopic characterizations and antioxidant capacity measurements. M.P. performed and analysed the assessment of the water accessibility of films. C.M. performed the AFM observations and surface topography analysis. B.G. and A.G-C. performed the antibacterial tests on cellulose-lignin films and interpreted the data. B.C. and A.M. prepared the derived lignin samples by ionic liquid treatment and performed the ^{31}P NMR measurements as D.C. on the lignin model compounds. The article was written by V.A—B, with important contributions from S.B. and M.Ö. All the authors read, reviewed and approved the final manuscript.

Acknowledgement

The authors thank Brigitte Chabbert (UMR FARE, Reims, France) and Michael Molinari (CBMN UMR CNRS 5248, Université de Bordeaux, IPB, Pessac, 33600, France) for their scientific support and fruitful discussion on lignin and AFM measurements, respectively; Dr. Raphael Coste for the complementary surface topography analysis by AFM, and the platforms Nano'mat, PLAneT of the University Reims-Champagne Ardennes, and the IJPB Institute Plant Observatory Chemistry and Metabolism Platform for access to AFM and NMR.

Author contributions section

V.A-B., B.K., S.B. and M.Ö. conceived the scientific strategy of the study within the framework of the Zelcor project, which is coordinated by S.B., E.G. and Y.M.F. performed the EPR measurements and interpreted the experimental data. G.N.R., L.F. and B.G. conceived of the cellulose films and performed their spectroscopic characterizations and antioxidant capacity measurements. M.P. performed and analysed the assessment of the water accessibility of films. C.M. performed the AFM observations and surface topography analysis. B.G. and A.G-C. performed the antibacterial tests on cellulose-lignin films.

Appendix A. Supplementary data

Supplementary data to this article can be found online at https://doi.org/10.1016/j.ijbiomac.2021.03.081.

References

[1] M.A. Hubbe, A. Ferrer, P. Tyagi, Y.Y. Yin, C. Salas, L. Pal, O.J. Rojas, Nanocellulose in thin films, coatings, and plies for packaging applications: a review, Bioresources 12(1) (2017) 2143–2233.

[2] E. Sourty, D.H. Ryan, R.H. Marchessault, Characterization of magnetic membranes based on bacterial and man-made cellulose, Cellulose 5(1) (1998) 5–17. doi: 10.1023/A:1009207027869.

[3] G. Kwon, K. Lee, D. Kim, Y. Jeon, U.J. Kim, J. You, Cellulose nanocrystal-coated TEMPO-oxidized cellulose nanofiber films for high performance all-cellulose nanocomposites, J. Hazard. Mater. 398 (2020)https://doi.org/10.1016/j.jhazmat.2020.123100.

[4] F. Jiang, A.R. Esker, M. Roman, Acid-catalyzed and solvolytic desulfation of H2SO4-hydrolyzed cellulose nanocrystals, Langmuir 26 (23) (2010) 17919–17925, https://doi.org/10.1021/la1028405.

[5] D. Klemm, F. Kramer, S. Moritz, T. Lindstrom, M. Ankerfors, D. Gray, A. Dorris, Nanocelluloses: a new family of nature-based materials, Angewandte Chemie-International Edition 50 (24) (2011) 5438–5466, https://doi.org/10.1002/anie.201001273.

[6] E. Kontturi, P. Laaksonen, M.B. Linder, Nonappa, A.H. Groschel, O.J. Rojas, O. Ikkala, Advanced materials through assembly of nanocelluloses, Adv. Mater. 30(24) (2018). doi:https://doi.org/10.1002/adma.201703779.

[7] X.Z. Xu, F. Liu, L. Jiang, J.Y. Zhu, D. Haagenson, D.P. Wiesenborn, Cellulose nanocrystals vs. cellulose nanofibrils: a comparative study on their microstructures and effects as polymer reinforcing agents, ACS Appl. Mater. Interfaces 5 (8) (2013) 2999–3009, https://doi.org/10.1021/am302624t.

[8] V. Aguié-Béghin, G. Païs, M. Molinari, B. Chabbert, Films and Coatings from Lignocellulosic Polymers, Edible Films and Coatings: Fundamentals and Applications, in: M. Pilar Montero Garcia (Ed.), Food Preservation Technology Series, CRC Press Taylor&Francis Group 2017, p. 598.

[9] N. Mittal, F. Ansari, V.K. Gowda, C. Brouzet, P. Chen, P.T. Larsson, S.V. Roth, F. Lundell, L. Wagberg, N.A. Kotov, L.D. Soderberg, Multiscale control of nanocellulose assembly: transferring remarkable nanoscale fibril mechanics to macroscale fibers, ACS Nano 12(7) (2018) 6378–6388. doi:https://doi.org/10.1021/acsnano.8b01084.

[10] R.J. Moon, A. Martini, J. Nairn, J. Simonsen, J. Youngblood, Cellulose nanomaterials review: structure, properties and nanocomposites, Chem. Soc. Rev. 40 (7) (2011) 3941–3994, https://doi.org/10.1039/C0CS00108B.
[11] Z.D. Zhu, S.Y. Fu, N. Lavoine, L.A. Lucia, Structural reconstruction strategies for the design of cellulose nanomaterials and aligned wood cellulose-based functional materials - a review, Carbohydr. Polym. 247 (2020)https://doi.org/10.1016/j.carbpol.2020.116722.
[12] R. Rinaldi, R. Jastrzebski, M.T. Clough, J. Ralph, M. Kennema, P.C.A. Bruijnincx, B.M. Weckhuysen, Paving the way for lignin valorisation: recent advances in bioengineering, biorefining and catalysis, Angewandte Chemie-International Edition 55 (29) (2016) 8164–8215, https://doi.org/10.1002/anie. 201510351.
[13] A. Grossman, W. Vermerris, Lignin-based polymers and nanomaterials, Curr. Opin. Biotechnol. 56 (2019) 112–120, https://doi.org/10.1016/j.copbio.2018.10.009.
[14] R. Singh, J.G. Hu, M.R. Regner, J.W. Round, J. Ralph, J.N. Saddler, L.D. Eltis, Enhanced delignification of steam-pretreated poplar by a bacterial laccase, Sci. Rep. 7 (2017) https://doi.org/10.1038/srep42121.
[15] T. Tokimatsu, S. Miyata, S.H. Ahn, T. Umezawa, T. Hattori, M. Shimada, Degradation of non-phenolic beta-O-4 type lignin carbohydrate complex model compounds by lignin peroxidase from the white-rot fungus Phanerochaete chrysosporium, Mokuzai Gakkaishi 42(2) (1996) 173–179.
[16] D.S. Bajwa, G. Pourhashem, A.H. Ullah, S.G. Bajwa, A concise review of current lignin production, applications, products and their environmental impact, Ind. Crop. Prod. 139 (2019)https://doi.org/10.1016/j.indcrop.2019.111526.
[17] S. Constant, H.L.J. Wienk, A.E. Frissen, P. de Peinder, R. Boelens, D.S. van Es, R.J.H. Grisel, B.M. Weckhuysen, W.J.J. Huijgen, R.J.A. Gosselink, P.C.A. Bruijnincx, New insights into the structure and composition of technical lignins: a comparative characterisation study, Green Chem. 18(9) (2016) 2651–2665. doi:https://doi.org/10.1039/c5gc03043a.
[18] D.L. Gall, J. Ralph, T.J. Donohue, D.R. Noguera, Biochemical transformation of lignin for deriving valued commodities from lignocellulose, Curr. Opin. Biotechnol. 45 (2017) 120–126, https://doi.org/10.1016/j.copbio.2017.02.015.
[19] T. Aro, P. Fatehi, Production and application of lignosulfonates and sulfonated lignin, Chemsuschem 10 (9) (2017) 1861–1877, https://doi.org/10.1002/cssc.201700082.
[20] M. Toikka, G. Brunow, Lignin-carbohydrate model compounds. Reactivity of methyl 3-O-(alpha-L-arabinofuranosyl)-beta-D-xylopyranoside and methyl beta-D-xylopyranoside towards a beta-O-4-quinone methide, Journal of the Chemical Society-Perkin Transactions 1 (13) (1999) 1877–1883. doi:10.1039/a900434c.
[21] T. Tokimatsu, T. Umezawa, M. Shimada, Synthesis of four diastereomeric lignin carbohydrate complexes (LCC) model compounds composed of a beta-0-4 lignin model linked to methyl beta-D-glucoside, Holzforschung 50(2) (1996) 156–160. doi:https://doi.org/10.1515/hfsg.1996.50.2.156.
[22] V. Aguié-Béghin, L. Foulon, P. Soto, D. Crônier, E. Corti, F. Legee, L. Cezard, B. Chabbert, M.N. Maillard, W.J.J. Huijgen, S. Baumberger, Use of food and packaging model matrices to investigate the antioxidant properties of biorefinery grass lignins, J. Agric. Food Chem. 63 (45) (2015) 10022–10031, https://doi.org/10.1021/acs.jafc.5b03686.
[23] A. Majira, B. Godon, L. Foulon, J.C. van der Putten, L. Cezard, M. Thierry, F. Pion, A. Bado-Nilles, P. Pandard, T. Jayabalan, V. Aguié-Béghin, P.H. Ducrot, C. Lapierre, G. Marlair, R.J.A. Gosselink, S. Baumberger, B. Cottyn, Enhancing the antioxidant activity of technical lignins by combining solvent fractionation and ionic-liquid treatment, Chemsuschem 12 (21) (2019) 4799–4809, https://doi.org/10.1002/cssc.201901916.
[24] M. Österberg, M.H. Sipponen, B.D. Mattos, O.J. Rojas, Spherical lignin particles: a review on their sustainability and applications, Green Chem. 22 (9) (2020) 2712–2733, https://doi.org/10.1039/d0gc00096e.
[25] S. Beisl, A. Friedl, A. Miltner, Lignin from micro- to nanosize: applications, Int. J. Mol. Sci. 18 (11) (2017)https://doi.org/10.3390/ijms18112367.
[26] M. Culebras, M.J. Sanchis, A. Beaucamp, M. Carsi, B.K. Kandola, A.R. Horrocks, G. Panzetti, C. Birkinshaw, M.N. Collins, Understanding the thermal and dielectric response of organosolv and modified Kraft lignin as a carbon fibre precursor, Green Chem. 20(19) (2018). doi:https://doi.org/10.1039/c8gc01577e/rsc.li/greenchem.
[27] H.L. Dong, M. Li, Y.C. Jin, Y. Wu, C.X. Huang, J.L. Yang, Preparation of graphene-like porous carbons with enhanced thermal conductivities from lignin nano-particles by combining hydrothermal carbonization and pyrolysis, Frontiers in Energy Research 8 (2020)https://doi.org/10.3389/fenrg.2020.00148.
[28] Y. Qian, X.Q. Qiu, X.W. Zhong, D.L. Zhang, Y.H. Deng, D.J. Yang, S.P. Zhu, Lignin reverse micelles for UV-absorbing and high mechanical performance thermoplastics, Ind. Eng. Chem. Res. 54 (48) (2015) 12025–12030, https://doi.org/10.1021/acs.iecr.5b03360.
[29] P. Ortiz-Serna, M. Carsi, M. Culebras, M.N. Collins, M.J. Sanchis, Exploring the role of lignin structure in molecular dynamics of lignin/bio-derived thermoplastic elastomer polyurethane blends, Int. J. Biol. Macromol. 158 (2020) 1369–1379, https://doi.org/10.1016/j.ijbiomac.2020.04.261.
[30] A. Hambardzumyan, L. Foulon, N.B. Bercu, M. Pernes, J.E. Maigret, M. Molinari, B. Chabbert, V. Aguié-Béghin, Organosolv lignin as natural grafting additive to improve the water resistance of films using cellulose nanocrystals, Chem. Eng. J. 264 (2015) 780–788, https://doi.org/10.1016/j.cej.2014.12.004.
[31] A. Hambardzumyan, L. Foulon, B. Chabbert, V. Aguié-Béghin, Natural organic UV-absorbent coatings based on cellulose and lignin: designed effects on spectroscopic properties, Biomacromolecules 13 (12) (2012) 4081–4088, https://doi.org/10.1021/bm301373b.
[32] M. Farooq, T. Zou, G. Rivière, M.H. Sipponen, M. Österberg, Strong, ductile, and waterproof cellulose nanofibril composite films with colloidal lignin particles, Biomacromolecules 20 (2) (2019) 693–704, https://doi.org/10.1021/acs.biomac.8b01364.
[33] A.P. Richter, J.S. Brown, B. Bharti, A. Wang, S. Gangwal, K. Houck, E.A.C. Hubal, V.N. Paunov, S.D. Stoyanov, O.D. Velev, An environmentally benign antimicrobial nanoparticle based on a silver-infused lignin core, Nat. Nanotechnol. 10(9) (2015) 817 doi:https://doi.org/10.1038/NNANO.2015.141.
[34] G.N. Rivière, A. Korpi, M.H. Sipponen, T. Zou, M.A. Kostiainen, M. Österberg, Agglomeration of viruses by cationic lignin particles for facilitated water purification, ACS Sustain. Chem. Eng. 8 (10) (2020) 4167–4177, https://doi.org/10.1021/acssuschemeng.9b06915.
[35] K. Kanomata, N. Fukuda, T. Miyata, P.Y. Lam, T. Takano, Y. Tobimatsu, T. Kitaoka, Lignin-inspired surface modification of nanocellulose by enzyme-catalyzed radical coupling of coniferyl alcohol in pickering emulsion, ACS Sustain. Chem. Eng. 8 (2) (2020) 1185–1194, https://doi.org/10.1021/acssuschemeng.9b06291.
[36] L. Bai, L.G. Greca, W.C. Xiang, J. Lehtonen, S.Q. Huan, R.W.N. Nugroho, B.L. Tardy, O.J. Rojas, Adsorption and assembly of cellulosic and lignin colloids at oil/water interfaces, Langmuir 35 (3) (2019) 571–588, https://doi.org/10.1021/acs.langmuir.8b01288.
[37] M.H. Sipponen, M. Smyth, T. Leskinen, L.S. Johansson, M. Österberg, All-lignin approach to prepare cationic colloidal lignin particles: stabilization of durable Pickering emulsions, Green Chem. 19 (24) (2017) 5831–5840, https://doi.org/10.1039/c7gc02900d.
[38] C.X. Huang, J.M. Ma, W.Y. Zhang, G. Huang, Q. Yong, Preparation of lignosulfonates from biorefinery lignins by sulfomethylation and their application as a water reducer for concrete, Polymers 10 (8) (2018)https://doi.org/10.3390/polym10080841.
[39] E. Gerbin, Y.M. Frapart, C. Marcuello, B. Cottyn, L. Foulon, M. Pernes, D. Crônier, M. Molinari, B. Chabbert, P.H. Ducrot, S. Baumberger, V. Aguié-Béghin, B. Kurek, Dual antioxidant properties and organic radical stabilization in cellulose nanocomposite films functionalized by in situ polymerization of coniferyl alcohol, Biomacromolecules 21 (8) (2020) 3163–3175, https://doi.org/10.1021/acs.biomac.0c00583.
[40] L. Zheng, P. Yu, Y. Zhang, P. Wang, W. Yan, B. Guo, C. Huang, Q. Jiang, Evaluating the bio-application of biomacromolecule of lignin-carbohydrate complexes (LCC) from wheat straw in bone metabolism via ROS scavenging, Int. J. Biol. Macromol. 176 (2021) 13–25, https://doi.org/10.1016/j.ijbiomac.2021.01.103.
[41] J.H. Lora, Lignin: a platform for renewable aromatic polymeric materials, Quality Living through Chemurgy and Green Chemistry2016, pp. 221–261.
[42] M. Österberg, J. Vartiainen, J. Lucenius, U. Hippi, J. Seppala, R. Serimaa, J. Laine, A fast method to produce strong NFC films as a platform for barrier and functional materials, ACS Appl. Mater. Interfaces 5 (11) (2013) 4640–4647, https://doi.org/10.1021/am401046x.
[43] C. Marcuello, L. Foulon, B. Chabbert, M. Molinari, V. Aguié-Béghin, Langmuir-Blodgett procedure to precisely control the coverage of functionalized AFM cantilevers for SMFS measurements: application with cellulose nanocrystals, Langmuir 34 (32) (2018) 9376–9386. doi:10.1021/acs.langmuir.8b01892.
[44] A. Granata, D.S. Argyropoulos, 2-Chloro-4,4,5,5-tetramethyl-1,3,2-dioxaphospholane, a reagent for the accurate determination of the uncondensed and condensed phenolic moieties in lignins, J. Agric. Food Chem. 43 (6) (1995) 1538–1544, https://doi.org/10.1021/jf00054a023.
[45] J.E. Sader, I. Larson, P. Mulvaney, L.R. White, Method for the calibration of atomic-force microscope cantilevers, Rev. Sci. Instrum. 66 (7) (1995) 3789–3798, https://doi.org/10.1063/1.1145439.
[46] K. Meinander, T.N. Jensen, S.B. Simonsen, S. Helveg, J.V. Lauritsen, Quantification of tip-broadening in non-contact atomic force microscopy with carbon nanotube tips, Nanotechnology 23 (40) (2012)https://doi.org/10.1088/0957-4484/23/40/405705.
[47] L. Muraille, M. Pernes, A. Habrant, R. Serimaa, M. Molinari, V. Aguié-Béghin, B. Chabbert, Impact of lignin on water sorption properties of bioinspired self-assemblies of lignocellulosic polymers, Eur. Polym. J. 64 (2015) 21–35, https://doi.org/10.1016/j.eurpolymj.2014.11.040.
[48] W. Brand-Williams, M.E. Cuvelier, C. Berset, Use of a free radical method to evaluate antioxidant activity, Lebensm.-Wiss. u.-Technol. 28 (1995) 25–30.
[49] R. Re, N. Pellegrini, A. Proteggente, A. Pannala, M. Yang, C. Rice-Evans, Antioxidant activity applying an improved ABTS radical cation decolorization assay, Free Radic. Biol. Med. 26 (9–10) (1999) 1231–1237, https://doi.org/10.1016/S0891-5849(98)00315-3.
[50] N. Pellegrini, F. Visioli, S. Buratti, F. Brighenti, Direct analysis of total antioxidant activity of olive oil and studies on the influence of heating, J. Agric. Food Chem. 49 (5) (2001) 2532–2538, https://doi.org/10.1021/jf001418j.
[51] V. Aguié-Béghin, S. Baumberger, B. Monties, R. Douillard, Formation and characterization of spread ligin layers at the air water interface, Langmuir 18 (2002) 5190–5196, https://doi.org/10.1021/la011766v.
[52] I. Boukari, J.L. Putaux, B. Cathala, A. Barakat, B. Saake, C. Remond, M. O'Donohue, B. Chabbert, In vitro model assemblies to study the impact of lignin-carbohydrate interactions on the enzymatic conversion of xylan, Biomacromolecules 10 (9) (2009) 2489–2498, https://doi.org/10.1021/bm9004518.
[53] T. Leskinen, M. Smyth, Y. Xiao, K. Lintinen, M.L. Mattinen, M.A. Kostiainen, P. Oinas, M. Österberg, Scaling up production of colloidal lignin particles, Nordic Pulp & Paper Research Journal 32(4) (2017) 586–596. doi:10.3183/NPPRJ-2017-32-04-p586-596.
[54] C. Marcuello, L. Foulon, B. Chabbert, V. Aguié-Béghin, M. Molinari, Atomic force microscopy reveals how relative humidity impacts the Young's modulus of lignocellulosic polymers and their adhesion with cellulose nanocrystals at the nanoscale, Int. J. Biol. Macromol. 147 (2020) 1064–1075, https://doi.org/10.1016/j.ijbiomac.2019.10.074.
[55] Z.D. Zhu, S.Y. Fu, L.A. Lucia, Tuning the morphology of microparticles from spray drying of cellulose nanocrystal suspensions by hydrophobic lignin, ACS Sustain. Chem. Eng. 7 (5) (2019) 5376–5384, https://doi.org/10.1021/acssuschemeng.8b06399.

[56] M. Montero-Munoz, J.E. Ramos-Ibarra, J.E. Rodriguez-Paez, G.E. Marques, M.D. Teodoro, J.A.H. Coaquira, Growth and formation mechanism of shape-selective preparation of ZnO structures: correlation of structural, vibrational and optical properties, Phys. Chem. Chem. Phys. 22 (14) (2020) 7329–7339, https://doi.org/10.1039/c9cp06744b.

[57] M.R. Benzigar, S. Joseph, G. Saianand, A.I. Gopalan, S. Sarkar, S. Srinivasan, D.H. Park, S. Kim, S.N. Talapaneni, K. Ramadass, A. Vinu, Highly ordered iron oxide-mesoporous fullerene nanocomposites for oxygen reduction reaction and supercapacitor applications, Microporous Mesoporous Mater. 285 (2019) 21–31, https://doi.org/10.1016/j.micromeso.2019.04.071.

[58] C.X. Huang, H.L. Dong, Z.P. Zhang, H.Y. Bian, Q. Yong, Procuring the nano-scale lignin in prehydrolyzate as ingredient to prepare cellulose nanofibril composite film with multiple functions, Cellulose 27 (16) (2020) 9355–9370, https://doi.org/10.1007/s10570-020-03427-9.

[59] N. Gierlinger, L. Goswami, M. Schmidt, I. Burgert, C. Coutand, T. Rogge, M. Schwanninger, In situ FT-IR microscopic study on enzymatic treatment of poplar wood cross-sections, Biomacromolecules 9 (8) (2008) 2194–2201, https://doi.org/10.1021/bm800300b.

[60] M. Schwanninger, J.C. Rodrigues, H. Pereira, B. Hinterstoisser, Effects of short-time vibratory ball milling on the shape of FT-IR spectra of wood and cellulose, Vib. Spectrosc. 36 (1) (2004) 23–40, https://doi.org/10.1016/j.vibspec.2004.02.003.

[61] I.V. Pylypchuk, P.A. Linden, M.E. Lindstrom, O. Sevastyanova, New insight into the surface structure of lignin nanoparticles revealed by H-1 liquid-state NMR spectroscopy, ACS Sustain. Chem. Eng. 8 (36) (2020) 13805–13812, https://doi.org/10.1021/acssuschemeng.0c05119.

[62] O. Faix, D.S. Argyropoulos, D. Robert, V. Neirinck, Determination of hydroxyl-groups in lignins evaluation of H-1-Nmr, C-13-Nmr, P-31-Nmr, Ftir and wet chemical methods, Holzforschung 48(5) (1994) 387–394. doi:https://doi.org/10.1515/hfsg.1994.48.5.387.

[63] K.M. Schaich, X. Tian, J. Xie, Hurdles and pitfalls in measuring antioxidant efficacy: a critical evaluation of ABTS, DPPH, and ORAC assays (reprinted), J. Funct. Foods 18 (2015) 782–796. doi:10.1016/j.jff.2015.05.024.

[64] S.S. Nair, J.Y. Zhu, Y.L. Deng, A.J. Ragauskas, Hydrogels prepared from cross-linked nanofibrillated cellulose, ACS Sustain. Chem. Eng. 2 (4) (2014) 772–780, https://doi.org/10.1021/sc400445t.

[65] K. Gabov, T. Oja, T. Deguchi, A. Fallarero, P. Fardim, Preparation, characterization and antimicrobial application of hybrid cellulose-lignin beads, Cellulose 24 (2) (2017) 641–658.

[66] J. Wang, W. Vermerris, Antimicrobial nanomaterials derived from natural products-a review, Materials 9(4) (2016). doi:10.1007/s10570-016-1172-y.

[67] J. Vachon, D. Assad-Alkhateb, S. Baumberger, J. van Haveren, R.J.A. Gosselink, Monedero, M., J.M. Bermudez, Use of lignin as additive in polyethylene for food protection: insect repelling effect of an ethyl acetate phenolic extract, Composites Part C.: Open Access 2 (2020) 100044 (2020) 1–9. doi:10.1016/j.jcomc.2020.100044.

[68] N.V. Loginova, H.I. Harbatsevich, N.P. Osipovich, G.A. Ksendzova, T.V. Koval'chuk, G.I. Polozov, Metal complexes as promising agents for biomedical applications, Curr. Med. Chem. 27 (31) (2020) 5213–5249, https://doi.org/10.2174/0929867326666190417143533.